



Synthesis of hematite ($\alpha\text{-Fe}_2\text{O}_3$) nanoparticles using *Syzygium cumini* extract: Photodegradation of norfloxacin and enhanced recyclability

Davi S. Ferreira ^a, Gleison N. Marques ^b, Adrianadas Mercês P. Ferreira ^c,
 Marcelo M. Oliveira ^{a,c}, Cláudia Q. da Rocha ^d, Ailton J. Moreira ^e, Carlos H.M. Fernandes ^f,
 Marcos R. Lanza ^f, Maria Inês B. Bernardi ^g, Lucia H. Mascaro ^b, José Hilton G. Rangel ^{a,c,*}

^a PPGQ – Federal Institute of Maranhão, Campus São Luís Monte Castelo – (IFMA), São Luís, MA, 65030-005, Brazil

^b CDMF, LIEC – Federal University of São Carlos – (UFSCar), São Carlos, SP, 13565-905, Brazil

^c PDQ – Federal Institute of Maranhão, Campus São Luís Monte Castelo – (IFMA), São Luís, MA, 65030-005, Brazil

^d PPGQuim-Federal University of Maranhão-(UFMA), São Luís, MA, 65080-805, Brazil

^e IQ – São Paulo State University (UNESP), Araraquara, SP, 14800-060, Brazil

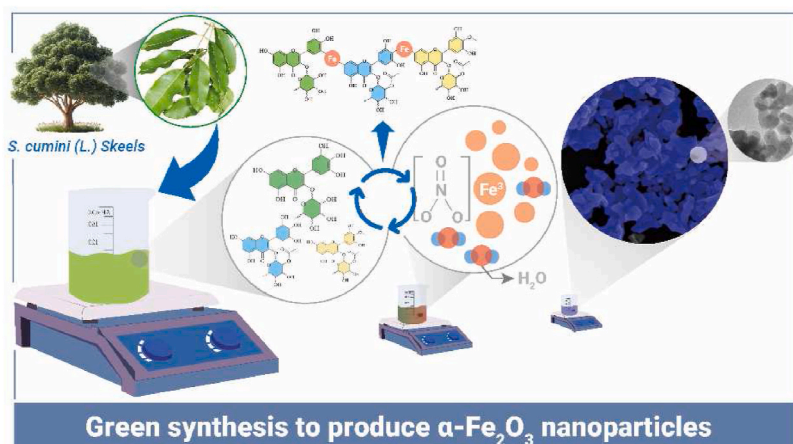
^f IQSC – University of São Paulo (IQSC-USP), São Carlos, SP, 13566-590, Brazil

^g IFSC – University of São Paulo (IFSC-USP), São Carlos, SP, 13560-970, Brazil

HIGHLIGHTS

- $\alpha\text{-Fe}_2\text{O}_3$ nanoparticles were produced by a green synthesis method using *Syzygium cumini* (L.) Skeels (Myrtaceae) leaf extract.
- The compounds present in the extract of *Syzygium cumini* (L.) Skeels were investigated by LC-ESI-ITMS.
- The morphology of the nanoparticles can be modified by the concentration of the extract and the heat treatment temperature.
- Photocatalytic efficiency of 96 % in 30 min of $\alpha\text{-Fe}_2\text{O}_3$ NPs in the degradation of Norfloxacin.

GRAPHICAL ABSTRACT



ARTICLE INFO

Keywords:

Norfloxacin
 Photodegradation
 $\alpha\text{-Fe}_2\text{O}_3$ nanoparticles
 Green synthesis
 Polyphenols

ABSTRACT

In this study, we report obtaining $\alpha\text{-Fe}_2\text{O}_3$ nanoparticles by a green synthesis method using different concentrations of *Syzygium cumini* (L.) Skeels (Myrtaceae) leaf extract. X-ray diffraction (XRD) analysis of materials confirmed the presence of pure hematite phase $\alpha\text{-Fe}_2\text{O}_3$ without any impurities. In addition, scanning electron microscopy (SEM) and transmission electron microscopy (TEM) techniques revealed almost spherical NPs' morphology. At the same time, it was clear from the dispersive energy X-ray (EDS) technique that no other chemical elements were present in the sample. On the other hand, the band gap energy obtained from the

* Corresponding author. PPGQ – Federal Institute of Maranhão, Campus São Luís Monte Castelo – (IFMA), São Luís, MA, 65030-005, Brazil.

E-mail address: hiltonrangel@ifma.edu.br (J.H.G. Rangel).

<https://doi.org/10.1016/j.matchemphys.2024.130281>

Received 7 October 2024; Received in revised form 21 November 2024; Accepted 12 December 2024

Available online 13 December 2024

0254-0584/© 2024 Elsevier B.V. All rights reserved, including those for text and data mining, AI training, and similar technologies.

materials was 1.9 and 2.0 eV. The photodegradation tests showed a photocatalytic efficiency of 96 % for the sample produced with the lowest extract concentration. The mineralization rate of norfloxacin was 32.5 %, as indicated by the Total Organic Carbon tests. In addition, its potential to generate reactive oxygen species that aid in the degradation of the pharmaceutical contaminant has been confirmed.

1. Introduction

The growing problems caused by the contamination of the environment by improperly disposed medicines, pesticides, and dyes have directly affected human health [1]. Among the primary contaminants in water bodies, pharmaceuticals are among the most harmful since antibiotics, for example, can accelerate the development of resistance mechanisms in bacteria of interest [2]. Among the antibiotics frequently found in aquatic bodies, Norfloxacin (NORF) is a widely used drug for fighting bacterial infections in humans and animals [3–5]. In this sense, several different methods have been used to degrade organic contaminants in aquatic environments [6–9]. On the other hand, the photocatalytic process mediated from nanometer-scale oxides represents one of the most efficient strategies for oxidizing organic pollutants [3,7].

Iron-based oxides are exciting due to their wide availability and unique properties, such as ferrimagnetism [10]. These magnetic properties have been exploited to assist in removing these materials from the aquatic environment after application [10–12]. Hematite ($\alpha\text{-Fe}_2\text{O}_3$) is a metal oxide widely used because it is environmentally safe, presents good stability, and possesses high photocatalytic capacity for degradation of organic compounds [13].

Like other oxides, the structural, optical, morphological, and magnetic properties of $\alpha\text{-Fe}_2\text{O}_3$ nanoparticles (NPs) can strongly influence their photocatalytic capacity [14–16]. An adjustable and simple synthesis method reflects the improvement of the properties of $\alpha\text{-Fe}_2\text{O}_3$ NPs [17,18]. Aalim and Shah [19] produced $\alpha\text{-Fe}_2\text{O}_3$ nanorods and nanospheres rich in oxygen vacancies after thermally processing the material produced by microwave irradiation. Zhang et al. [20] produced mesoporous $\alpha\text{-Fe}_2\text{O}_3$ nanorods by controlling the addition of NaOH through a hydrothermal process followed by heat treatment. Compared with the same material's microplates, the nanorods showed high photocatalytic capacity and good recyclability in tests involving the degradation of methylene blue under visible light.

Recently, synthesis approaches based on extracts from plant parts such as leaves, stems, and fruits have gained special attention [21–26]. Much of the interest in these compounds is the possibility of replacing toxic and expensive reagents with molecules that can reduce and stabilize metal ions. This happens through the capping process of the nanoparticles produced, thus avoiding ultra-agglomeration [18,23]. Among the various plants used in biosynthesis, *Syzygium cumini* is a plant that presents several chemical constituents and phytochemical compounds, such as tannins, alkaloids, steroids, flavonoids, terpenoids, fatty acids, and vitamins [18].

Recently, our research group achieved essential breakthroughs in synthesizing Fe-doped SnO_2 using the alcoholic extract of the leaves of *Syzygium cumini* [27]. It was shown that the phytochemical compounds present in the extract acted as a chelating and capping agent for the nanoparticles. In addition, the materials produced had a relatively high concentration of tin and oxygen vacancies. Riaz et al. [18] also reported the production of NiO nanoparticles (NiO-NPs) using *Syzygium cumini* extract. These green synthesis NPs showed high removal efficiency for the dyes congo red and methylene blue and good antioxidant capacity.

Therefore, this study investigated obtaining $\alpha\text{-Fe}_2\text{O}_3$ NPs using different concentrations of the alcoholic extract of *S. cumini* (*L.*) *Skeels* (17.5 and 22.5 g). The photocatalytic activity of these NPs was evaluated using NORF as the actual molecule in the photodegradation tests. Recyclability tests were also carried out to check the integrity of the catalyst, and a degradation mechanism was proposed.

2. Experimental section

2.1. Synthesis of nanomaterials

2.1.1. Materials

70 % ethanol (Itajá) was used to prepare the hydroalcoholic extract of *S. cumini* (*L.*) *Skeels*. For the synthesis of the oxides, iron (III) nitrate nonahydrate ($\text{Fe}(\text{NO}_3)_3 \cdot 9\text{H}_2\text{O}$ - Sigma-Aldrich, 98 %) was used. The norfloxacin (NORF, $\text{C}_{16}\text{H}_{18}\text{FN}_3\text{O}_3$ - Sigma-Aldrich – 99.5 %) was used in the photodegradation assays. None of the reagents used underwent any purification.

2.1.2. Extract production

The leaves of *S. cumini* collected at the State University of Maranhão ($2^\circ 34' 53.7''$ S $44^\circ 12' 28.8''$ W) were washed with double distilled water to remove impurities. Then, the leaves were dried in an oven with air circulation at 60°C for 48 h. After this step, the leaves were ground in a cyclone-type rotor mill (TE – 651/2) using a 20-mesh. For the preparation of the extract, different proportions (17.5 and 22.5 g) of the previously ground leaves were added in an Erlenmeyer containing 100 mL of 70 % ethyl alcohol and kept under constant agitation at 100 rpm for a period of 48 h on a shaker table. After this period, the extract was vacuum-filtered and stored to synthesize the oxides.

For the HPLC (High-Performance Liquid Chromatography) analysis, the extract was cleaned by solid phase extraction (SPE) using Strata C-18 silica cartridges (500mg/6 mL - Phenomenex) activated with 3 mL of methanol (MeOH) [28]. Then, 0.0060 g of the alcoholic extract was dissolved in 1.0 mL of MeOH and transferred to the SPE cartridge (6 mL), and eluted with 1.0 mL of MeOH. Subsequently, the samples underwent a drying process and resolubilization in 1.0 mL MeOH to be filtered through a $0.45\ \mu\text{m}$ polypropylene microfilter. Chemical characterization was performed by LC-ESI-IT-MS with a spectrometer (Bruker, Massachusetts, EUA). The chromatographic analysis was performed on a Luna $5\ \mu\text{m}$ C18 100 Å column ($250 \times 4.6\ \text{mm}$, Phenomenex, Torrance, EUA). The binary gradient mobile phase consisted of 0.1 % formic acid (Sigma-Aldrich, St. Louis, LO, USA) in water (solvent A) and 0.1 % formic acid in methanol (Sigma-Aldrich, St. Louis, LO, USA) (solvent B). Compounds were eluted from the analytical column with a 90 min gradient ranging from 5 % to 100 % solvent B at a constant $1\ \text{mL min}^{-1}$ flow rate. Column compartment temperature set to 25°C . Data acquisition was performed in positive and negative ionization mode, with fragmentation in multiple stages (MS^2 and MS^3), according to the following parameters: nebulization gas pressure, 50.0 psi; capillary temperature, 300°C ; transfer capillary input voltage, $-4500\ \text{V}$; desolvation gas, Nitrogen (N_2), flow $10\ \text{L min}^{-1}$; collision gas, Helium (He); range acquisition, m/z 50–1200. Raw data were analyzed using Data Analysis 4.3 software (Bruker, Massachusetts, EUA).

2.1.3. Synthesis of $\alpha\text{-Fe}_2\text{O}_3$

To evaluate the influence of *S. cumini* (*L.*) *Skeels* extract concentration on $\alpha\text{-Fe}_2\text{O}_3$ production; powders were synthesized by solubilizing $0.025\ \text{mol Fe}(\text{NO}_3)_3 \cdot 9\text{H}_2\text{O}$ in 100 mL of the two different extract concentrations (17.5 and 22.5 %). The solution containing the metallic precursor and the extract was stirred and heated at 60°C until a highly viscous gel was formed. After this step, the material was dried in an oven at 100°C for 24 h and then deagglomerated in an agate mortar. Finally, the dried material was calcined at 500 and 650°C in a muffle furnace for 2 h at a heating rate of $10^\circ\text{C min}^{-1}$. The samples were designated A1 (Extract concentration - 17.5 % and NP heat treatment temperature –

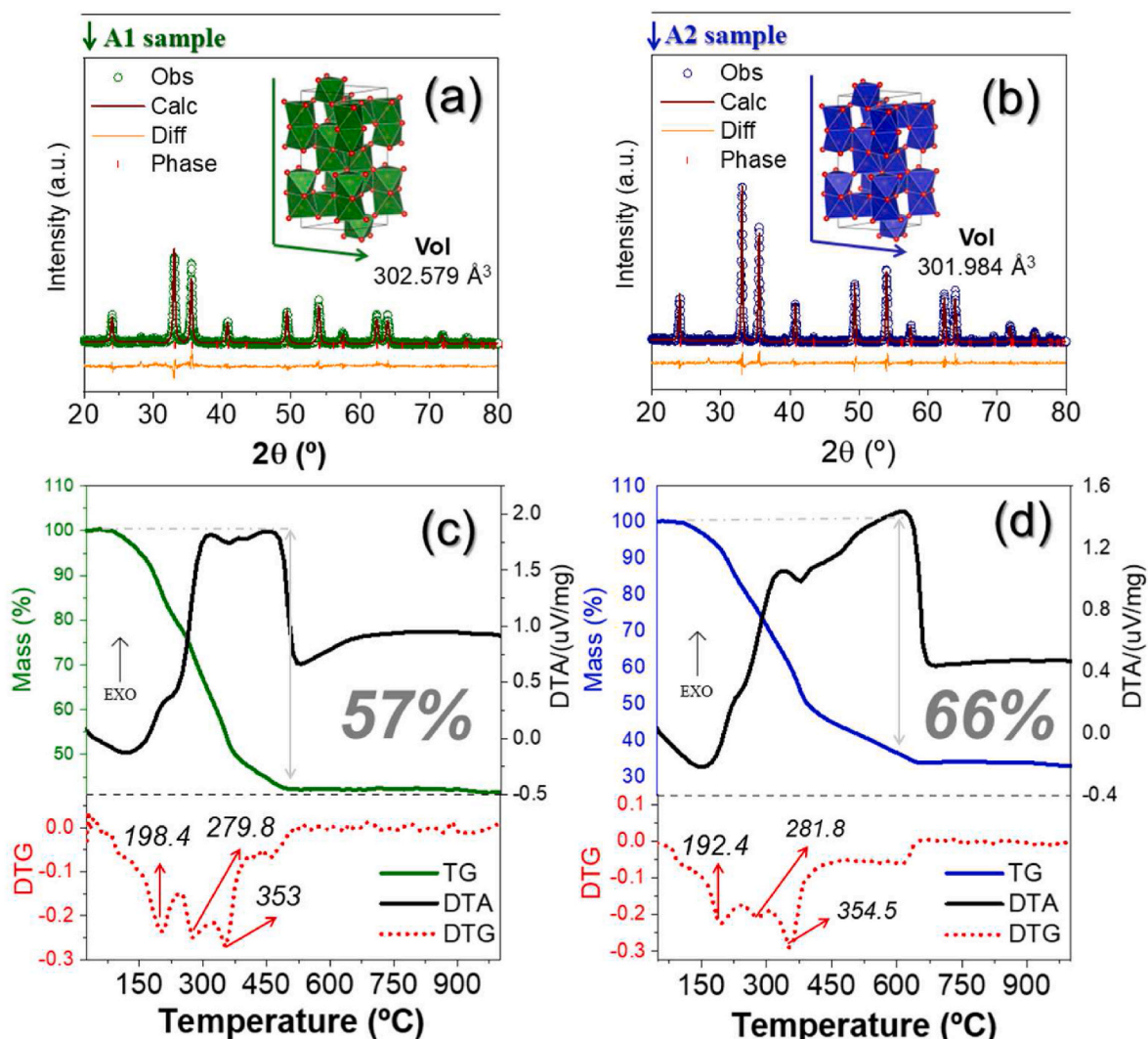


Fig. 1. (a–b) X-ray diffractograms and (c–d) TG/DTA curves of α -Fe₂O₃-NPs.

500 °C) and A2 (Extract concentration - 22.5 % and NP heat treatment temperature – 650 °C).

2.2. Characterization techniques

The powders produced were characterized by Thermogravimetric – Differential Thermal Analysis (TGA-DTA) using Netzsch equipment, model 409 Cell, with a heating rate of 10 °C min⁻¹, in the temperature range between 25 and 1000 °C in an oxidizing atmosphere (compressed air). The structural analysis was carried out by X-ray diffraction (XRD) using a Shimadzu diffractometer (XRD 6100), operating with CuK α radiation ($\lambda = 1.5415 \text{ \AA}$), with an acceleration voltage of 40 kV and 30 mA of current. The scanning rate was 10° min⁻¹ with a step size of 0.05° and a range of 10–110° (2 θ). Calculations of the phase composition and determination of the network parameters were carried out using Rietveld refinement using the GSAS software with the EXPGUI interface [29]. The crystallite sizes were obtained from the Scherrer (Eq. (1)) and Williamson-Hall equations (Eq. (2)).

$$T_c = \frac{k\lambda}{\beta \cos \theta} \quad \text{Eq. 1}$$

Where T_c corresponds to the size of the crystallite, k is Scherrer's constant, which varies between 0.85 and 0.9 depending on the shape of the crystallite (here 0.89 was considered), λ is the wavelength of the

radiation used in the equipment, β is the full width at half height (FWHM) of the diffraction peak, and θ is the Bragg angle. In the Williamson-Hall equation (Eq. (2)), ϵ represents the deformation of the crystalline lattice and D the size of the crystallite, and both values can be obtained from the slope and intercept of the line originating from the graph of $\beta_{hkl} \cos \theta$ by $4 \epsilon \sin \theta$ [30].

$$\beta_{hkl} \cos \theta = \frac{k\lambda}{D} + 4\epsilon \sin \theta \quad \text{Eq. 2}$$

The Fourier Transform Infrared (FTIR) technique was used to study the chemical bonds in materials based on the vibration they present after absorbing energy. To this end, tablets containing approximately 1 % of each α -Fe₂O₃ powder and 99 % potassium bromide (KBr-99 %, Sigma Aldrich) were produced. The measurements were carried out on a Shimadzu spectrophotometer (IRA Ffinity-1) between 400 and 4000 cm⁻¹. Diffuse reflectance data was obtained using a UV–Vis spectrophotometer (CARY 70000 - AGILENT) in the 200–800 nm wavelength range. The morphological characteristics of the nanomaterials were investigated by scanning electron microscopy using a field emission scanning electron microscope (SEM-FEG), model Supra 35 VP from Zeiss. The morphology of the Fe₂O₃ was analyzed using the transmission electron microscopy (TEM) technique on an FEI TECNAI F20 microscope (Netherlands) operating at 200 kV. The compositional analysis used the energy dispersive X-ray spectroscopy (EDS) technique using a Quanta 450 – FEI equipped with sensors EDS/EBSD. The Brunauer, Emmett, and Teller

Table 1

Crystallite size obtained by the Scherrer and Williamson-Hall equations, lattice parameters, and Rietveld refinement reliability factors.

samples	Crystallite size		Lattice parameter				Rietveld agreement factors ^a	
	Scherer	W-H	a (Å)	b (Å)	c (Å)	V (Å ³)	R _{wp}	χ ²
A1	28.51	24.67	5.04	5.04	13.76	349.52	21.2	1.869
A2	37.64	34.32	5.04	5.04	13.75	349.27	19.43	1.537

^a The XRD data were refined using CIF #ICSD 85177 as a reference.

(BET) method determined the specific surface area through nitrogen adsorption and desorption using a NOVA 2200 device (Quantachrome Instruments).

2.3. Photocatalysis experiments

For photodegradation assays, 50 mg of the catalyst was added to 50 mL of NORF standard solution at a concentration of 50 mg L⁻¹ and left for 3 min in an ultrasonic bath to fully disperse the powder. The samples were then taken to a wooden reactor equipped with 6 lamps. The samples were kept in the dark for 30 min under constant stirring to reach adsorption-desorption equilibrium. After this stage, the solution was irradiated with UV light (254 nm - Osram, 15 W). Aliquots of 1 mL were taken at 5, 10, 15, 30, 45, 60, and 90 min, centrifuged, filtered using Nylon membrane filters (porosity 0.45 μm), and analyzed by high-pressure liquid chromatography (HPLC).

The HPLC analyses to monitor degradation were carried out using a Shimadzu chromatograph, model 20A, consisting of two LC-20AD pumps, an SPD-20AD UV-Vis detector, and a SIL-20AD automatic injector, managed by a CBM-20AD controller. The chromatographic measurement conditions for the elution of NORF considered the mobile phase, a mixture of 50 % (v/v) acetonitrile and water in a 50:50 ratio, using a flow rate of 1.0 mL min⁻¹; the stationary phase, a Kinetex C18-Phenomenex column (reverse phase), composed of 5 μm particles, with an internal diameter of 4.60 mm and a length of 150 mm. The injection temperature and analysis volume were 23 °C and 25 μL, respectively. According to these chromatographic conditions, the NORF molecule shows an absorption peak at λ = 280 nm with a retention time of around 2–2.5 min. A calibration curve was constructed to obtain a linear relationship between the concentration of NORF and the chromatographic peak area in the concentration range from 1.5 to 100 mg L⁻¹. The NORF removal efficiency was calculated using Eq. (3), where C is the final concentration, and C₀ is the initial concentration of NORF.

$$\text{Removal efficiency (\%)} = 100 \cdot \left(1 - \frac{C}{C_0}\right) \quad \text{Eq. 3}$$

A scavenger assay using the sample with the best results was carried out by studying the photocatalytic inhibition resulting from the capture of reactive oxygen species. For this, 0.7 mg of ascorbic acid -AA (Isifar, 99 %), 0.64 mg of silver nitrate -AgNO₃ (Isifar, 99 %), 3.4 mL of *tert*-butyl alcohol - TBA (Neon, 99 %), and 0.56 mg ammonium oxalate - AO (Sigma-Aldrich, 99 %) were used as •O₂⁻, e⁻, •OH and h⁺ scavengers, respectively. For the catalyst reuse test, the material was washed with distilled water after each cycle, dried in an oven at 100 °C for 1 h, and reused [31,32].

3. Results and discussion

3.1. Structural, morphological, and compositional characterization

The X-ray pattern of samples A1 and A2 (Fig. 1a–b) showed prominent peaks centered on 2θ = 33.04°, characteristic of the hematite phase (α-Fe₂O₃). The rhombohedral structure belonging to space group R-3c (n° 167), characteristic of this phase, also corroborates the specifications of the JCPDS 033-0664 crystallographic patterns. Heat treatment at 500 or 650 °C for A1 or A2, respectively, increased the

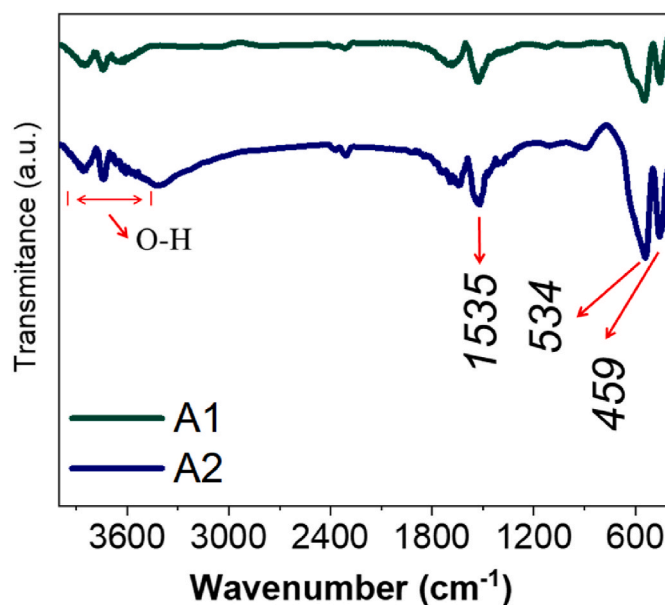


Fig. 2. FTIR spectra of Fe₂O₃-NPs NPs produced with *S. cumini* (*L.*) Skeels extract at 17.5 and 22.5 % concentrations at 500 and 650 °C, respectively.

crystallinity of the materials to values of around 54.8 % in A1 and 66.3 % in A2. This is because the presence of organic extract induces the amorphous nature of the materials. The crystallite size, which represents the first stage in the formation of the nanomaterials, was 28.51 nm for A1 and 37.64 nm for A2. As the crystallization stage begins during heat treatment at 100 °C for 24 h, it can be said that the smaller amount of extracts in A1 was responsible for producing materials with reduced crystallite sizes. This is because the extract encapsulates the crystals in formation [18,33], giving rise to different crystallization nuclei, which result in small crystallites. Considering the crystallite size values obtained using the Scherrer equation, it was observed that A2 had a crystal size 24 % larger than A1. However, this is still smaller than in the literature, confirming that the extract induces a reduction in crystal size due to the encapsulation mechanism [34]. The crystallite size values calculated using Williamson-Hall follow the same behavior as the values observed by Scherrer but still follow the increasing behavior between A1 and A2 (Table 1).

From the refinement calculations of the crystalline network of both samples, a slight contraction in the volume of the lattice was observed, which may be associated with the effect of temperature on the processing of the material (Table 1). The R_{wp} and χ² reliability parameter values confirm the accuracy of the data. Still, when heat-treated at high temperatures (500 or 650 °C), the decomposition of the extract is accompanied by the more efficient crystallization of the metal oxide. The TG/DTA and DTG curves of the samples (Fig. 1c–d) showed a thermal event between 50 and 150 °C, which can be attributed to the loss of water adsorbed on the material's surface [14,35]. The events observed between 150 °C and 640 °C are attributed to the decomposition of the organic extract [36,37], which results in a mass loss of 57 and 66 % in samples A1 and A2, respectively. From the DTA curves, which are superimposed on the mass loss events, the first thermal event is an

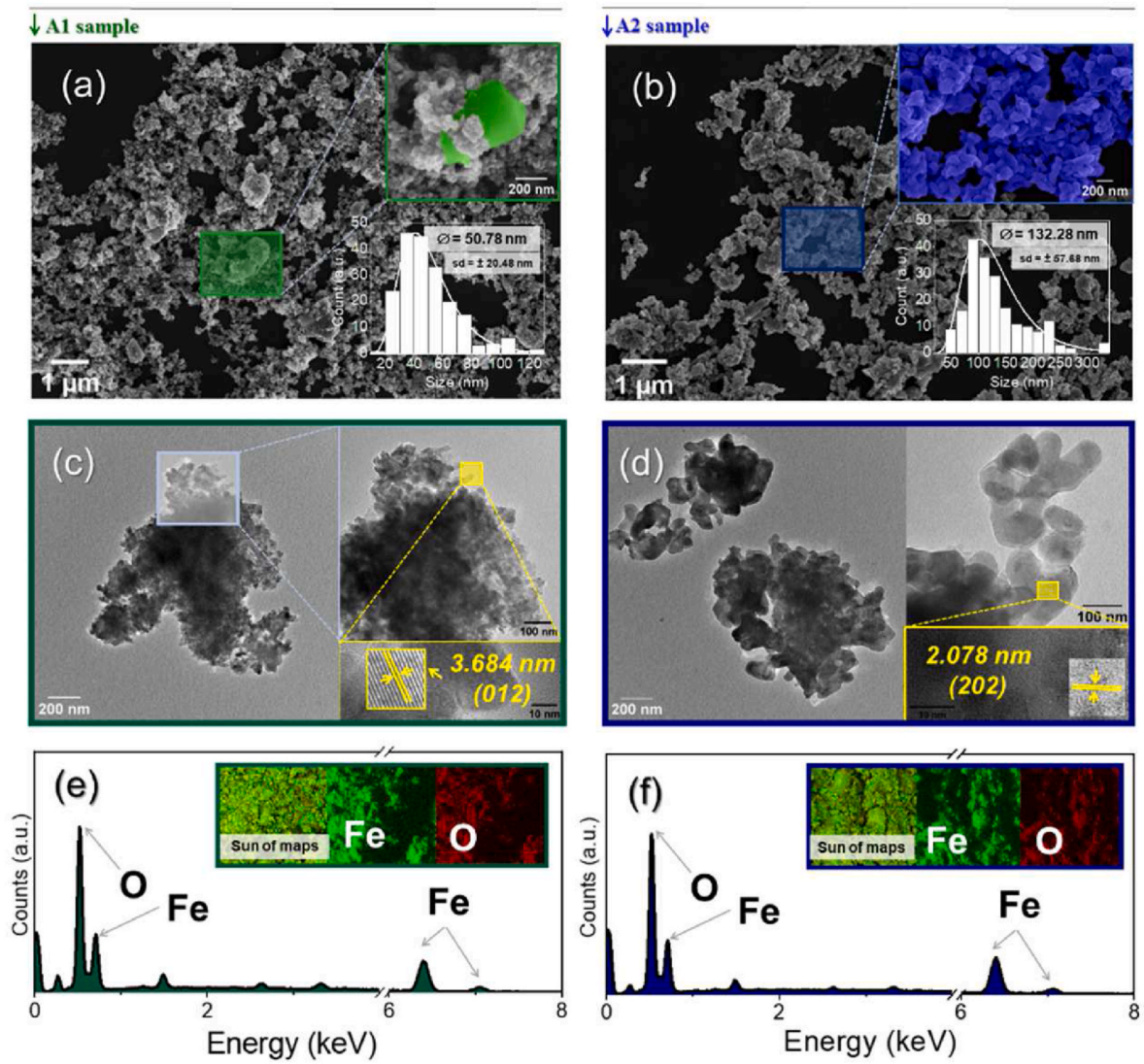


Fig. 3. (a–b) SEM images and insert with histograms of the average particle sizes, (c–d) TEM images with an insert of the high-resolution TEM micrographs, and (e–f) EDS spectra of samples.

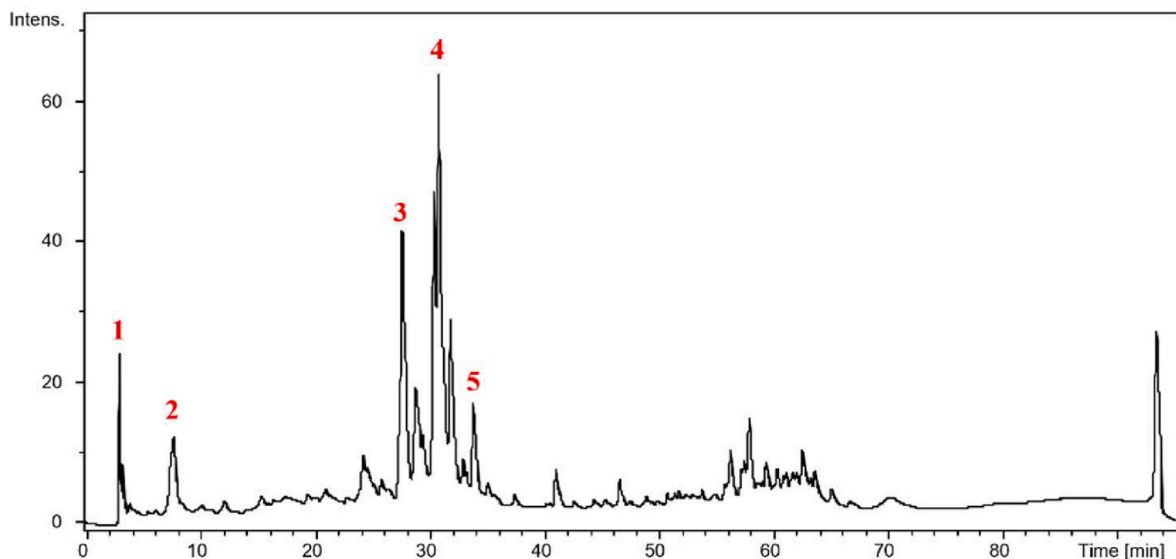
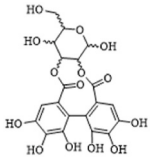
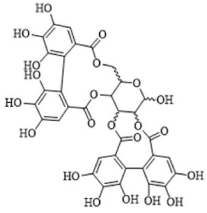
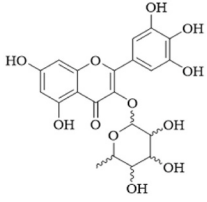
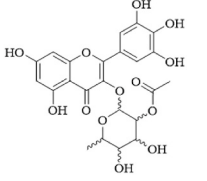
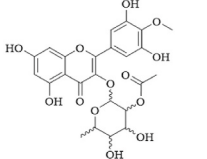


Fig. 4. Chromatogram of the HPLC-UV analysis of the ethanolic extract of *Syzigium cumini*.

Table 2Annotation of compounds obtained from the ethanolic extract of *Syzygium cumini* analyzed by HPLC-MS-MS.

Peak	Retention time (min)	Compound	ESI (-)/MS/MS fragments	Molecular structure	Reference
1	3.1	HHDP-hexoside	481 [M-H] ⁻ /301; 275		[41–43]
2	7.8	Bis-HHDP-hexoside	783 [M-H] ⁻ /763; 481; 301; 275		[41,44,45]
3	27.7	myricetin 3-O-deoxyhexoside	463 [M-H] ⁻ /316; 271; 179		[46–48]
4	31.8	myricetin 3-O-acetyl-deoxyhexoside	505 [M-H] ⁻ /463; 316; 271; 179		[42,49]
5	33.7	4-methylmyricetin-3-O-acetyldeoxyhexoside	519 [M-H] ⁻ /504; 577; 477; 331; 315; 287		[41,42]

endothermic activity corresponding to the loss of water, and the other events are exothermic, indicating the combustion of organic matter, leaving only the presence of α -Fe₂O₃.

The FTIR spectra shown in Fig. 2 indicate the presence of bands in the range between 3958 and 3622 cm⁻¹, which can be attributed to the vibrations of the O - H bond related to the water adsorbed on the surface of the material [21,38]. The bands observed at 534 and 459 cm⁻¹ are attributed to the Fe - O [21,39]. Narrow bands were also observed between 1700 and 1300 cm⁻¹, corresponding to the C=C and C - N bonds in aromatic compounds and amide groups [21,39]. The more intense transmittance peaks observed for sample A1 confirm that the extract residue persists in the material due to the lower heat treatment temperature (500 °C) than sample A2 (650 °C).

The morphology of samples A1 (Fig. 3a–c) and A2 (Fig. 3b–d) observed by SEM-FEG and TEM showed particles with a tendency towards a spherical shape and different sizes. Sample A1 has an average diameter of 50.78 ± 20.48 nm, and sample A2 has a diameter of 132.28 ± 57.68 nm. The standard deviation values for the particle size of samples A1 and A2 were 40 % and 44 % of the calculated average diameter, respectively. This shows a high degree of particle diameter heterogeneity, so the extract concentration effect was not attributed. However, the larger particle diameter of sample A2 can be attributed to the higher heat treatment temperature (650 °C). In this condition, the thermal decomposition of the extract increases the coalescence of

particles, giving rise to a larger diameter particles.

HR-TEM images reveal the presence of network bands with interplanar spacing that correspond to the (202) and (012) planes (Insert in Fig. 3c–d), corroborating the JCPDS file (033–0664) indexed from the XRD diffraction data. EDS compositional analysis (Fig. 3e–f) revealed the presence of the elements Fe (green) and O (red). The additional peaks observed in the spectrum refer to the elements Al and C present in the sample holder and carbon tape, respectively.

To better understand how the extract acts in the process of nucleation and formation of α -Fe₂O₃-NPs, it is first necessary to elucidate the phytochemicals present in the extract of the leaves of *S. cumini* (L.) Skeels [40]. In this sense, Fig. 4 shows the chromatogram obtained from the HPLC analysis of ethanolic extract. Numerous peaks were observed, indicating a complex mixture of compounds within the extract. For detailed characterization, the peaks with the highest intensity and retention times below 40 min (specifically Peaks 1, 2, 3, 4, and 5) were selected for further analysis by mass spectrometry. These peaks were prioritized due to their prominent signals in the HPLC-PDA analysis, suggesting they represent the main constituents of the extract and are likely key components contributing to its bioactivity and chemical profile.

The LC-MS/MS analysis of the extract revealed that the predominant peaks correspond to high molecular weight compounds, primarily identified as phenolic compounds rich in hydroxyl groups characteristic

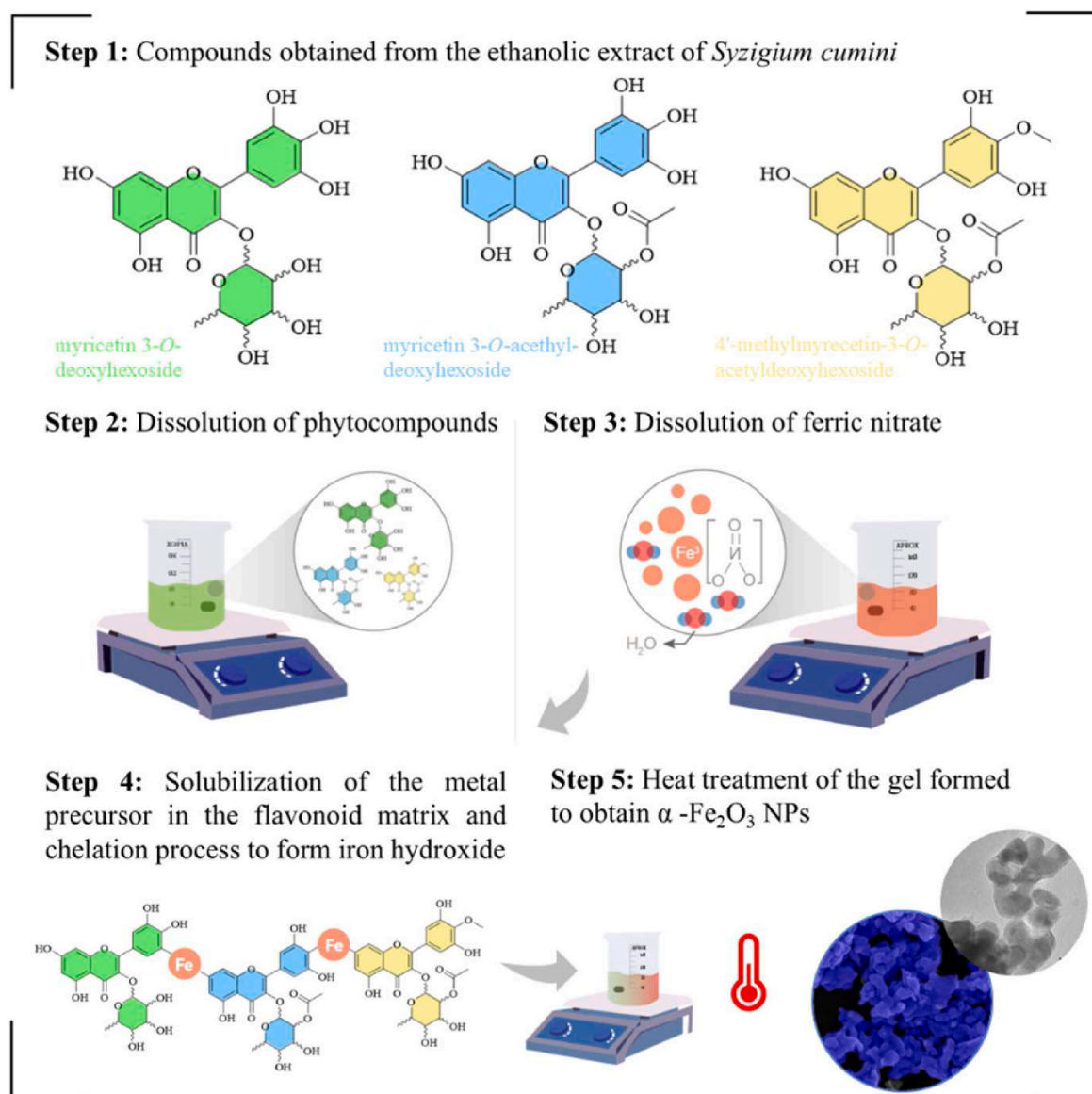


Fig. 5. Schematic illustration of the mechanism of formation of α -Fe₂O₃ NPs from green synthesis using phytochemicals present in the extract of the leaves of *S. cumini* (*L.*) *Skeels*. (For interpretation of the references to colour in this figure legend, the reader is referred to the Web version of this article.)

of their respective organic functions. In addition to hydroxyl groups, these compounds exhibit a diverse array of functional groups, including alcohol, ketone, ether, and ester functionalities, as outlined in Table 2. This multifunctional composition suggests a complex structure that could contribute to the extract's reactivity and potential applications in synthesis and other chemical processes [41].

The extract, characterized by a high concentration of polyphenol compounds, serves as an effective alternative to ethylene glycol for the synthesis of nanomaterials [50,51]. Its composition allows it to function not only as a solvent but also as an encapsulating agent that facilitates the controlled growth of nanocrystals, providing precise control over their size and morphology [52]. In addition, the structural properties of certain compounds such as quercetin and myricetin confer chelating capabilities, allowing the sequestration of metal precursor ions during synthesis [52–55]. In this sense, some studies suggest that the main mechanism involved in the process of producing nanoparticles by green synthesis is the initial oxidation of the hydroxyl group in these molecules [54]. In our preliminary investigation to determine the phytochemicals present in the extract, three different myricetin molecules were observed (myricetin 3-O-deoxyhexoside, myricetin

3-O-acetyl-deoxyhexoside, and 4'-methylmyricetin-3-O-acetyldeoxyhexoside). A possible mechanism involved in the production of α -Fe₂O₃ NPs is shown in Fig. 5. After oxidizing the hydroxyl groups of these three molecules, the next step is the reduction of the previously solubilized Fe ions (Fig. 5) [54]. The process ends with the chelation of Fe in the phytocomposite matrix for subsequent calcination and obtaining of α -Fe₂O₃ NPs powders.

Fig. 6 shows the N₂ adsorption/desorption isotherms for the Fe₂O₃ samples. The specific surface area presented for samples A1 and A2 was 46 and 16 m² g⁻¹, respectively. The porosity of the materials, analyzed by the nitrogen adsorption isotherms, and the pore size distribution obtained by the Barrett-Joyner-Halenda (BJH) method was 11.7 nm (A1) and 2.4 nm (A2). The synthesized oxides showed a type IV isotherm with a H3 hysteresis loop. This type of isotherm occurs when there is capillary condensation of the mesopores, while the H3-type hysteresis loop is due to aggregates of non-rigid plate-like particles or macropores that have not been filled with pore condensates [56,57].

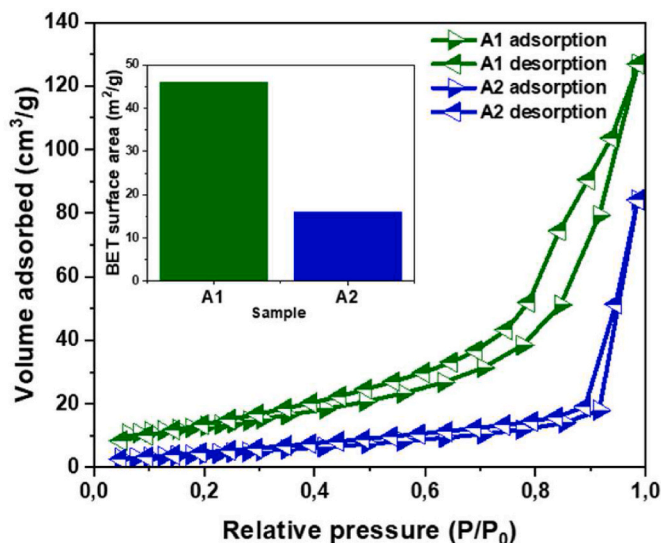


Fig. 6. N_2 gas adsorption-desorption isotherms of $\alpha\text{-Fe}_2\text{O}_3$ samples. The BET surface area of the two samples is inset.

3.2. Optical properties and photodegradation assays of norfloxacin

Fig. 7a–b shows the band gap values of the samples obtained by extrapolating the curves from the Tauc graph. The band gap values were determined using the Kubelka-Munk method [58] (Eq. (4)).

$$\alpha h\nu = A(h\nu - E_g)^n \quad \text{Eq. 4}$$

Where α represents the linear absorption coefficient of the material, h corresponds to the energy of the incident photon, A is the proportionality constant, E_g is the bandgap energy of the material, and n is a constant referring to the type of electronic transition of the material in question. The value of n can be $\frac{1}{2}$ if the transition is a direct allowed transition or 2 if it is an indirect allowed transition. The values of 1.9 and 2.0 eV for samples A1 and A2, respectively, align with others found in the literature [15]. This difference, although small, is probably related to a size and/or shape effect [59]. The reflectance band observed in the UV-Vis graphs (Insert Fig. 7a–b) may be related to the charge transfer process after excitation of the hole-electron (e^-/h^+) pair. In addition, the band observed at ~ 610 nm may indicate an excellent ability to capture light energy due to oxygen vacancy defects [60].

As shown in Fig. 7c–e, in 30 min, NORF degradation reaches 96 % efficiency. As adsorptive removal is an important process in the photocatalytic mechanism, the adsorption contribution of samples A1 and A2 was ~ 49 and 41 %, respectively (Fig. 7c). This result confirms that the surface of the materials has a high capacity to interact with the organic molecule due to the presence of functional groups from the extract. The degradation kinetics showed a good fit to the pseudo-first-order model, and the observed kinetic constant values $k_{\text{Obs}} = 9.44 \times 10^{-3} \text{ min}^{-1}/R^2 = 0.763$, for photolysis, and $k_{\text{Obs}} = 5.69 \times 10^{-2} \text{ min}^{-1}/R^2 = 0.998$, and $k_{\text{Obs}} = 2.068 \times 10^{-2} \text{ min}^{-1}/R^2 = 0.956$, A1 and A2, respectively. The photooxidation capacity of NORF using A1 and its mineralization was confirmed through TOC assays, where the mineralization rate achieved was around 32.5 %. In comparison, the sample resulting from photolysis was only 4.6 %. Fig. 5f shows that material A1 lost approximately 15 % of its photodegradation capacity even after 270 min of testing, which confirms its high recyclability.

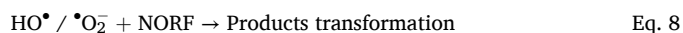
The photocatalytic degradation of Norfloxacin in this work was compared with the performance of other materials reported in the literature, and the data were grouped in Table 3. In some cases, such as the formation of Fe_2O_3 - TiO_2 microporous structures and TiO_2/Ti films, the performance of the Fe_2O_3 produced here was superior when comparing the concentrations of NORF at which the studies showed the

best results [61,62].

Assays to capture reactive oxygen species (ROS) generated by the interaction of light with the catalyst surface were carried out under the same conditions as the photocatalytic tests but using sample A1. As is well known, photocatalytic degradation reactions occur on the catalyst's surface. The mechanism is initiated by the formation of the electron (e^-)/hole (h^+) pair after the electronic excitation of $\alpha\text{-Fe}_2\text{O}_3$, as represented in Eq. (5) [68].



As illustrated in Fig. 8, the h^+ species interact with the water adsorbed on the catalyst surface and generate hydroxyl radical (HO^\bullet). On the other hand, the electron that has migrated from VB to CB interacts with dissolved oxygen (O_2) and forms the superoxide radical ($^{\bullet}\text{O}_2^-$), as represented in Equations (6)–(8), respectively [68,69]. Both species generated are essential for the oxidation and mineralization processes of NORF [69].



The addition of AA and AgNO_3 as $^{\bullet}\text{O}_2^-$ and e^- probes showed no significant reduction in photocatalytic activity (Fig. 8b). Eq. (9) shows the reaction that occurred after the addition of TBA to the system, which results in a decrease in the material's degradation efficiency, considering that HO^\bullet is an essential oxidizing agent in the NORF oxidation process in the presence of $\alpha\text{-Fe}_2\text{O}_3$.



Some previous studies using TBA as a probe for HO^\bullet observed a suppression rate of the radicals and suggested that volume may influence the ability to suppress the corresponding species [70]. Adding AO as an h^+ capture agent reduced the rate of NORF degradation, indicating that this is the most important species in the photocatalytic process.

In this sense, both the structural and morphological data and the photocatalytic application of these NPs confirm the efficiency of the *S. cumini* extract as a reducing and encapsulating agent. This is a point that deserves a lot of attention, especially in the sense that this extract can be used to produce other functionalized NPs such as ZnO, NiO, CuO, and WO_3 for various applications [71–74].

4. Conclusion

This work successfully synthesizes $\alpha\text{-Fe}_2\text{O}_3$ NPs using different concentrations of *S. cumini* extract. The XRD patterns showed that the material presented only $\alpha\text{-Fe}_2\text{O}_3$ phases. Different concentrations of extract associated with the temperature difference influenced the morphological modification of the materials, especially the degree of aggregation and particle size. The photocatalytic activity of the material was demonstrated based on assays using NORF, which showed a rate of $2.868 \times 10^{-2} \pm 0.019, \text{ min}^{-1}$ for the sample produced with 28 % more extract (A1). TOC tests revealed a mineralization rate of ~ 32 % of the drug-treated with sample A1. In addition, the material also showed high stability after 3 successive cycles under the same photodegradation conditions. On the other hand, the scavenger tests showed that the primary photodegradation mechanism of $\alpha\text{-Fe}_2\text{O}_3$ NPs is the generation of h^+ , followed by the production of $\bullet\text{OH}$ hydroxyl radicals. As a result, it can be concluded that iron oxides can be obtained by using *S. cumini* extract. Its concentration can affect the generation of defects on the surface of the materials and thus improve their photocatalytic performance.

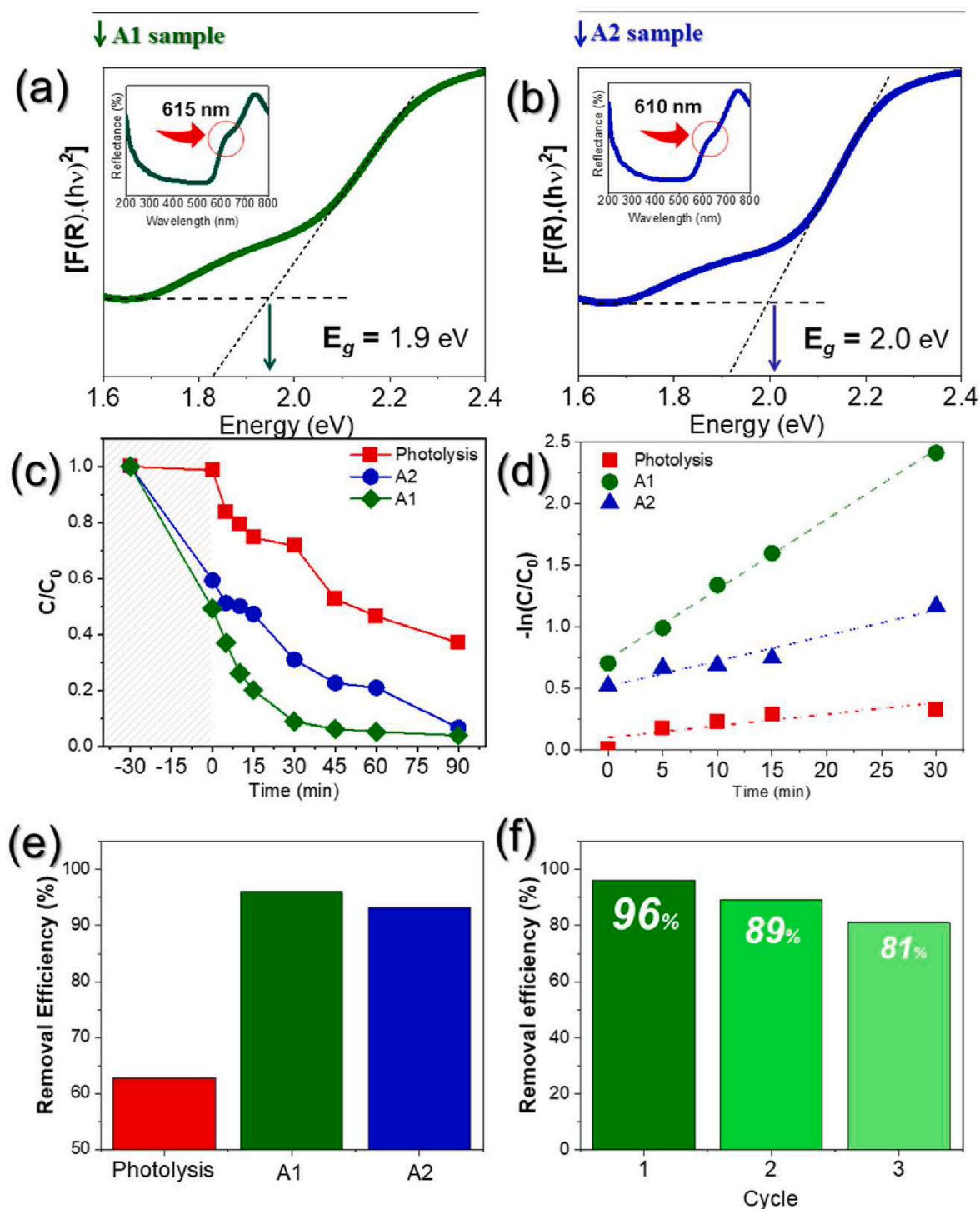


Fig. 7. Band gap and insertion of the DRS diffuse reflectance spectrum (a) A1, (b) A2 samples, (c) NORF removal rate as a function of time, (d) kinetic adjustment of the degradation rate to obtain K_{Obs} , and (e-f) NORF removal efficiency after repeated test cycles.

CRedit authorship contribution statement

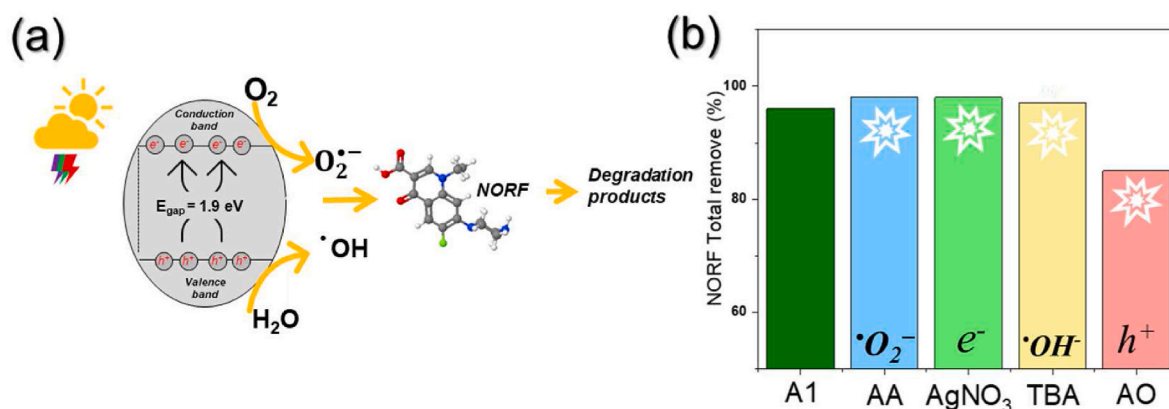
Davi S. Ferreira: Writing – original draft, Methodology, Investigation, Formal analysis, Conceptualization. **Gleison N. Marques:** Software, Investigation, Formal analysis, Data curation, Conceptualization. **Adrianadas Mercês P. Ferreira:** Investigation, Data curation, Conceptualization. **Marcelo M. Oliveira:** Writing – review & editing, Validation, Supervision. **Cláudia Q. da Rocha:** Data curation, Formal analysis, Investigation, Software, Writing – review & editing. **Ailton J. Moreira:** Writing – review & editing, Visualization, Validation,

Investigation, Conceptualization. **Carlos H.M. Fernandes:** Visualization, Validation, Investigation, Conceptualization. **Marcos R. Lanza:** Writing – review & editing, Visualization, Validation. **Maria Inês B. Bernardi:** Writing – review & editing, Visualization, Validation. **Lucia H. Mascaro:** Writing – review & editing, Visualization, Validation, Data curation. **José Hilton G. Rangel:** Writing – review & editing, Visualization, Validation, Supervision, Resources, Project administration, Funding acquisition, Data curation.

Table 3

Comparison of the photocatalytic efficiency of different catalysts against NORF.

Photocatalyst	Amount of loaded catalyst (mg)	pH	NORF concentration (mg/L)	Light source	Time (min)	Degradation efficiency (%)	Ref.
Fe ₂ O ₃ – TiO ₂	500	7	10	UV-light	90	100	[61]
ZnO/ZnS@BC	500	7	25	UV-light	180	95	[63]
TiO ₂ /Ti Films	–	–	10	UV-light	90	98	[62]
Co–Cu ₂ O	60	–	19.13	Xenon lamp 500 W	210	82.23	[64]
Cu/Ni ₂ O ₃ @PC	25	5	20	UV-light	180	59.2	[65]
Mn: ZnS quantum dots	60	10	15	UV-light	60	86	[66]
BiOCl nanosheets	50	–	10	Xenon lamp 300 W with an AM 1.5 filter	180	84	[67]
α-Fe ₂ O ₃	50	–	50	UV-light	90	96	This work

Fig. 8. (a) Proposed mechanism for the photodegradation of NORF using α -Fe₂O₃ and (b) scavenger tests using AA, AgNO₃, TBA, and AO.

Declaration of competing interest

The authors declare that they have no known competing financial interests or personal relationships that could have appeared to influence the work reported in this paper.

Acknowledgments

The authors gratefully acknowledge the assistance provided by IFMA, FAPESP (Grants and #2021/06128-5, #2023/01425-7, #2023/07525-3, #2022/06219-3, #2018/09761-8, #2018/22210-0, #2018/22211-7, #2018/22022-0, #2019/06650-3, #2022/12895-1 and #2023/06558-5), FAPESP/CEPID (#2013/07296-2), CNPq (#116926/2022-8), FAPEMA and CAPES (#88887.626035/2021-00 and 88887.472618/2019-00) finance code 001 in support of this research. We would also like to thank the Center for Development of Functional Materials (CDMF) and the Graduate Program in Materials Engineering at the Federal Institute of Maranhão (PPGEM-IFMA) for granting us access to their facilities.

Data availability

Data will be made available on request.

References

- [1] J. Toe, E. Orok, P. Erah, Assessment of knowledge and disposal practices of unused and expired household medicines in a community in Liberia, *Exploratory Research in Clinical and Social Pharmacy* 12 (2023) 100369, <https://doi.org/10.1016/j.rcsop.2023.100369>.
- [2] Ł. Sikorski, A. Beşbe, Effects of two pharmaceuticals: doxycycline and norfloxacin on plant and animal organisms living in the freshwater. <https://doi.org/10.1016/j.ecohyd.2024.02.007>, 2024.
- [3] K.G. Pavithra S K P, J. V, R.P. S, Removal of colorants from wastewater: a review on sources and treatment strategies, *J. Ind. Eng. Chem.* 75 (2019) 1–19, <https://doi.org/10.1016/j.jiec.2019.02.011>.
- [4] Q. Ma, N. Zhao, Y. Wei, S. Wang, D. Liu, P. Yuan, Efficient adsorption and separation of norfloxacin from water by allophane aerogel microspheres, *Sep. Purif. Technol.* 327 (2023) 124808, <https://doi.org/10.1016/j.seppur.2023.124808>.
- [5] S.L. Zhou, S. Zhang, F. Liu, J.J. Liu, J.J. Xue, D.J. Yang, C.T. Chang, ZnO nanoflowers photocatalysis of norfloxacin: effect of triangular silver nanoplates and water matrix on degradation rates, *J. Photochem. Photobiol. Chem.* 328 (2016) 97–104, <https://doi.org/10.1016/j.jphotochem.2016.03.037>.
- [6] T.H. Bokhari, A. Iqbal, M. Usman, M. Al Huwayz, M. Iqbal, A. Ali, N. Alwadai, M. Iqbal, A. Nazir, U. Younas, Gamma radiation-induced degradation of Acid Violet 49 in the presence of hydrogen peroxide (H₂O₂) in an aqueous medium, *Zeitschrift Fur Physikalische Chemie* (2024), <https://doi.org/10.1515/ZPCH-2022-0165/MACHINEREADEABLECITATION/RIS>.
- [7] M. Amjad, I. Bibi, F. Majid, K. Jilani, M. Sultan, Q. Raza, A. Ghafoor, N. Alwadai, A. Nazir, M. Iqbal, NiO/MnFe₂O₄ nanocomposite photoluminescence, structural, morphological, magnetic, and optical properties: photocatalytic removal of cresol red under visible light irradiation, *ACS Omega* 9 (2024) 20876–20890, https://doi.org/10.1021/ACSOMEGA.3C09637/SUPPL_FILE/AO3C09637_SI_001.PDF.
- [8] S. Fatima, M. Iqbal, H.N. Bhatti, N. Alwadai, M. Al Huwayz, A. Nazir, M. Iqbal, Kinetics and thermodynamics studies of nickel manganite nanoparticle as photocatalyst and fuel additive, *Heliyon* 10 (2024) e33861, <https://doi.org/10.1016/j.heliyon.2024.E33861>.
- [9] M. Akhtar, I. Bibi, F. Majid, A. Ghafoor, S. Kamal, G. Fatima, Q. Raza, N. Alwadai, A. Nazir, M. Iqbal, Photoluminescence, structural, optical, ferroelectric and photocatalytic properties of magnetically separable CdO/CoFe₂O₄ hetero-junction, *Ceram. Int.* 50 (2024) 13573–13581, <https://doi.org/10.1016/j.ceramint.2024.01.272>.
- [10] D.R. Rosaline, C. Keerthana, S.S. Vasthi, S.H. Rubini, J.H. Ratna Monica, A. Manikandan, S. Ashok Kumar, S.S.R. Inbanathan, A. Dinesh, K. Thanrasu, K. K. Raja, M.A. Almessiere, Y. Slimani, A. Baykal, A. Khan, A.M. Asiri, V. Gupta, Magnetic nanoparticles and nanocomposites for the applications of photocatalytic degradation of organic dyes, *Magnetic Nanoparticles and Polymer Nanocomposites* (2024) 459–497, <https://doi.org/10.1016/B978-0-323-85748-2.00018-9>.
- [11] E.C. Paris, J.O.D. Malafatti, A.J. Moreira, L.C. Santos, C.R. Scienna, A. Zenatti, M. T. Escote, V.R. Mastelaro, M.R. Joya, CuO nanoparticles decorated on hydroxyapatite/ferrite magnetic support: photocatalysis, cytotoxicity, and antimicrobial response, *Environ. Sci. Pollut. Control Ser.* 29 (2022) 41505–41519, <https://doi.org/10.1007/S11356-021-18263-Y/FIGURES/11>.

- [12] E.C. Paris, J.O.D. Malafatti, C.R. Sciena, L.F.N. Junior, A. Zenatti, M.T. Escote, A. J. Moreira, G.P.G. Freschi, Nb2O5 nanoparticles decorated with magnetic ferrites for wastewater photocatalytic remediation, *Environ. Sci. Pollut. Control Ser.* 28 (2021) 23731–23741, <https://doi.org/10.1007/S11356-020-11262-5/FIGURES/9>.
- [13] Z. Cao, M. Qin, B. Jia, Y. Gu, X. Wang, X. Qu, Facile synthesis of mesoporous hematite/carbon nanosheet for superior photodegradation, *J. Phys. Chem. Solid.* 107 (2017) 42–49, <https://doi.org/10.1016/J.JPCS.2017.02.017>.
- [14] M. Tadic, L. Kopanja, M. Panjan, J. Lazovic, B.V. Tadic, B. Stanojevic, L. Motte, Rhombohedron and plate-like hematite (α -Fe2O3) nanoparticles: synthesis, structure, morphology, magnetic properties and potential biomedical applications for MRI, *Mater. Res. Bull.* 133 (2021) 111055, <https://doi.org/10.1016/j.materresbull.2020.111055>.
- [15] W. Huang, X. Lu, D. Jia, J. Huang, Z. Li, H. Xie, M. Wang, Y. Li, D. Zhang, Characterization of structural, optical and photocatalytic properties of yttrium modified hematite (α -Fe2O3) nanocatalyst, *Ceram. Int.* 49 (2023) 25602–25611, <https://doi.org/10.1016/j.ceramint.2023.05.101>.
- [16] H. Han, T. Han, Y. Luo, M.A. Mushtaq, Y. Jia, C. Liu, Recent advances in α -Fe2O3-based photocatalysts for CO2 conversion to solar fuels, *J. Ind. Eng. Chem.* (2023), <https://doi.org/10.1016/j.jiec.2023.07.064>.
- [17] R. Padmavathi, R. Raja, C. Kalaiavanan, S. Kalaiselvan, Syzygium Cumini leaf extract exploited in the green synthesis of zinc oxide nanoparticles for dye degradation and antimicrobial studies, *Mater. Today Proc.* 69 (2022) 1200–1205, <https://doi.org/10.1016/j.matpr.2022.08.257>.
- [18] T. Riaz, A. Munwar, T. Shahzadi, M. Zaib, S. Shahid, M. Javed, S. Iqbal, K. Rizwan, M. Waqas, B. Khalid, N.S. Awwad, H.A. Ibrahim, M.A. Bajaber, Phyto-mediated synthesis of nickel oxide (NiO) nanoparticles using leaves' extract of Syzygium cumini for antioxidant and dyes removal studies from wastewater, *Inorg. Chem. Commun.* 142 (2022) 109656, <https://doi.org/10.1016/j.inoche.2022.109656>.
- [19] M. Aalim, M.A. Shah, Role of oxygen vacancies and porosity in enhancing the electrochemical properties of Microwave synthesized hematite (α -Fe2O3) nanostructures for supercapacitor application, *Vacuum* 210 (2023) 111903, <https://doi.org/10.1016/j.vacuum.2023.111903>.
- [20] G.-Y. Zhang, Y. Feng, Y.-Y. Xu, D.-Z. Gao, Y.-Q. Sun, Controlled synthesis of mesoporous α -Fe2O3 nanorods and visible light photocatalytic property, *Mater. Res. Bull.* 47 (2012) 625–630, <https://doi.org/10.1016/j.materresbull.2011.12.032>.
- [21] D. Sanap, L. Avhad, S. Ghotekar, N.D. Gaikwad, Green synthesis and characterization of mixed-phase Fe2O3 nanorods as a novel magnetically recoverable heterogeneous catalyst for Biginelli synthesis, *J. Mol. Struct.* 1283 (2023) 135246, <https://doi.org/10.1016/j.molstruc.2023.135246>.
- [22] P. Herrera-Marín, L. Fernández, F. Pilaquinca, F. A. Debut, A. Rodríguez, P. Espinoza-Montero, Green synthesis of silver nanoparticles using aqueous extract of the leaves of fine aroma cocoa Theobroma cacao linneu (Malvaceae): optimization by electrochemical techniques, *Electrochim. Acta* 447 (2023) 142122, <https://doi.org/10.1016/j.electacta.2023.142122>.
- [23] M. Khatun, Z. Khatun, MdR. Karim, MdR. Habib, MdH. Rahman, MdA. Aziz, Green synthesis of silver nanoparticles using extracts of Mikania cordata leaves and evaluation of their antioxidant, antimicrobial and cytotoxic properties, *Food Chemistry Advances* 3 (2023) 100386, <https://doi.org/10.1016/j.focha.2023.100386>.
- [24] A.T. Khalil, M. Ovais, I. Ullah, M. Ali, Z. Khan Shinwari, M. Maaza, Biosynthesis of iron oxide (Fe2O3) nanoparticles via aqueous extracts of Sageretia thea (Osbeck.) and their pharmacognostic properties, *Green Chem. Lett. Rev.* 10 (2017) 186–201, <https://doi.org/10.1080/17518253.2017.1339831>.
- [25] S.O. Aisida, N. Madubuonu, M.H. Alnasir, I. Ahmad, S. Botha, M. Maaza, F. I. Ezema, S.O. Aisida, N. Madubuonu, M.H. Alnasir, I. Ahmad, S. Botha, M. Maaza, F.I. Ezema, Biogenic synthesis of iron oxide nanorods using Moringa oleifera leaf extract for antibacterial applications, *ApNan* 10 (2019) 305–315, <https://doi.org/10.1007/S13204-019-01099-X>.
- [26] N. Madubuonu, S.O. Aisida, A. Ali, I. Ahmad, T. kai Zhao, S. Botha, M. Maaza, F. I. Ezema, Biosynthesis of iron oxide nanoparticles via a composite of Psidium guajava-Moringa oleifera and their antibacterial and photocatalytic study, *J. Photochem. Photobiol., B* 199 (2019) 111601, <https://doi.org/10.1016/J.JPHOTOBIO.2019.111601>.
- [27] M.H. da Silva Ribeiro, G.N. Marques, A.J. Moreira, M.M. Oliveira, R.C. Oliveira, R. T. da Silva, A.C. Krohling, W.A.A. Macedo, M.I.B. Bernardi, L.H. Mascaro, J.H. G. Rangel, H.B. de Carvalho, Green-assisted synthesis of highly defective nanostructured Fe-doped SnO2: magnetic and photocatalytic properties evaluation, *Acta Mater.* 277 (2024) 120194, <https://doi.org/10.1016/J.ACTAMAT.2024.120194>.
- [28] E. Hakme, M.E. Poulsen, Evaluation of the automated micro-solid phase extraction clean-up system for the analysis of pesticide residues in cereals by gas chromatography-Orbitrap mass spectrometry, *J. Chromatogr. A* 1652 (2021) 462384, <https://doi.org/10.1016/J.CHROMA.2021.462384>.
- [29] B.H. Toby, EXPGUI, a Graphical User Interface for GSAS, vol. 34, *Urn-Issn*, 2001, pp. 210–213, <https://doi.org/10.1107/S0021889801002242>, 0021-8898.
- [30] M. Ghasemi Hajiabadi, M. Zamanian, D. Souri, Williamson-Hall analysis in evaluation of lattice strain and the density of lattice dislocation for nanometer scaled ZnSe and ZnSe:Cu particles, *Ceram. Int.* 45 (2019) 14084–14089, <https://doi.org/10.1016/j.ceramint.2019.04.107>.
- [31] M.L. Barbosa, M.J.S. Costa, A.E.B. Lima, A.M. Batista, E. Longo, L.S. Cavalcante, R. S. Santos, Anionic and cationic dyes removal by degradation via photoelectrocatalysis using a WO3/CuWO4 heterojunction film as a photoanode, *Nano-Structures & Nano-Objects* 35 (2023) 100993, <https://doi.org/10.1016/j.nanoso.2023.100993>.
- [32] A.E.B. Lima, R.Y.N. Reis, L.S. Ribeiro, L.K. Ribeiro, M. Assis, R.S. Santos, C.H. M. Fernandes, L.S. Cavalcante, E. Longo, J.A.O. Osajima, G.E. Luz, Microwave-assisted hydrothermal synthesis of CuWO4-palygorskite nanocomposite for enhanced visible photocatalytic response, *J. Alloys Compd.* 863 (2021) 158731, <https://doi.org/10.1016/J.JALLCOM.2021.158731>.
- [33] R. Vinayagam, S. Pai, T. Varadavenkatesan, M.K. Narasimhan, S. Narayanasamy, R. Selvaraj, Structural characterization of green synthesized α -Fe2O3 nanoparticles using the leaf extract of Spondias dulcis, *Surface. Interfac.* 20 (2020) 100618, <https://doi.org/10.1016/j.surfin.2020.100618>.
- [34] P. Kumar, S. Kumar, N. Thakur, Azadirachta indica and polyvinylpyrrolidone encapsulated Fe2O3 nanoparticles to enhance the photocatalytic and antioxidant activity, *Inorg. Chem. Commun.* 155 (2023) 111084, <https://doi.org/10.1016/j.inoche.2023.111084>.
- [35] S. Kumar, A. Kumar, T. Malhotra, S. Verma, Characterization of structural, optical and photocatalytic properties of silver modified hematite (α -FeO) nanocatalyst, *J. Alloys Compd.* 904 (2022) 164006, <https://doi.org/10.1016/j.jallcom.2022.164006>.
- [36] M.F. Al-Hakkani, G.A. Gouda, S.H.A. Hassan, A.M. Nagiub, Echinacea purpurea mediated hematite nanoparticles (α -HNP) biofabrication, characterization, physicochemical properties, and its in-vitro biocompatibility evaluation, *Surface. Interfac.* 24 (2021) 101113, <https://doi.org/10.1016/j.surfin.2021.101113>.
- [37] D. Sharma, L. Ledwani, T. Mehrotra, N. Kumar, N. Pervaiz, R. Kumar, Biosynthesis of hematite nanoparticles using Rheum emodi and their antimicrobial and anticancerous effects in vitro, *J. Photochem. Photobiol., B* 206 (2020) 111841, <https://doi.org/10.1016/j.jphotobiol.2020.111841>.
- [38] MdS.H. Bhuiyan, M.Y. Miah, S.C. Paul, T. Das Aka, O. Saha, MdM. Rahaman, MdJ. I. Sharif, O. Habiba, Md Ashaduzzaman, Green synthesis of iron oxide nanoparticle using Carica papaya leaf extract: application for photocatalytic degradation of remazol yellow RR dye and antibacterial activity, *Heliyon* 6 (2020) e04603, <https://doi.org/10.1016/j.heliyon.2020.e04603>.
- [39] N. Srivastava, M. Srivastava, A. Alhazmi, A. Mohammad, S. Khan, D.B. Pal, S. Haque, R. Singh, P.K. Mishra, V.K. Gupta, Sustainable green approach to synthesize Fe3O4/ α -Fe2O3 nanocomposite using waste pulp of Syzygium cumini and its application in functional stability of microbial cellulases, *Sci. Rep.* 11 (2021) 24371, <https://doi.org/10.1038/s41598-021-03776-w>.
- [40] N. Matinise, X.G. Fuku, K. Kaviyarasu, N. Mayedwa, M. Maaza, ZnO nanoparticles via Moringa oleifera green synthesis: physical properties & mechanism of formation, *Appl. Surf. Sci.* 406 (2017) 339–347, <https://doi.org/10.1016/J.APSUSC.2017.01.219>.
- [41] A. Gordon, E. Jungfer, B.A. Da Silva, J.G.S. Maia, F. Marx, Phenolic constituents and antioxidant capacity of four underutilized fruits from the amazon region, *J. Agric. Food Chem.* 59 (2011) 7688–7699, <https://doi.org/10.1021/JF201039R>.
- [42] J.R. Sanches, L.M. França, V.T. Chagas, R.S. Gaspar, K.A. dos Santos, L. M. Gonçalves, D.M. Sloboda, A.C. Holloway, R.P. Dutra, E.M. Carneiro, A.P. G. Cappelli, A.M. de A. Paes, Polyphenol-rich extract of Syzygium cumini leaf dually improves peripheral insulin sensitivity and pancreatic islet function in monosodium L-glutamate-induced obese rats, *Front. Pharmacol.* 7 (2016) 172040, <https://doi.org/10.3389/FPHAR.2016.00048/BIBTEX>.
- [43] S. Tokuyama-Nakai, H. Kimura, Y. Hirabayashi, T. Ishihara, M. Jisaka, K. Yokota, Constituents of flavonol O-glycosides and antioxidant activities of extracts from seeds, sprouts, and aerial parts of Polygonum tinctorium Lour, *Heliyon* 5 (2019) e01317, <https://doi.org/10.1016/j.heliyon.2019.e01317>.
- [44] I.F. Pérez-Ramírez, R. Reynoso-Camacho, F. Saura-Calixto, J. Pérez-Jiménez, Comprehensive characterization of extractable and nonextractable phenolic compounds by high-performance liquid chromatography-electrospray ionization-quadrupole time-of-flight of a grape/pomegranate pomace dietary supplement, *J. Agric. Food Chem.* 66 (2018) 661–673, https://doi.org/10.1021/ACS.JAFC.7B05901/SUPPL_FILE/JF7B05901_SI_001.PDF.
- [45] C. dos Santos, R.S. Galaverna, C.F.F. Angolini, V.V.A. Nunes, L.F.R. de Almeida, A. L.T.G. Ruiz, J.E. de Carvalho, R.M.T. Duarte, M.C.T. Duarte, M.N.E. Eberlin, Antioxidative, antiproliferative and antimicrobial activities of phenolic compounds from three myrcia species, *Molecules* 23 (2018) 986, <https://doi.org/10.3390/MOLECULES23050986>, 2018, Vol. 23, Page 986.
- [46] V.T. Chagas, R.M.R. De Sousa Coelho, R.S. Gaspar, S.A. Da Silva, M. Mastrogiovanni, C. De Jesus Mendonça, M.N. De Souza Ribeiro, A.M. De Andrade Paes, A. Trostchansky, Protective effects of a polyphenol-rich extract from Syzygium cumini (L.) Skeels leaf on oxidative stress-induced diabetic rats, *Oxid. Med. Cell. Longev.* 2018 (2018) 5386079, <https://doi.org/10.1155/2018/5386079>.
- [47] E.J. Llorent-Martínez, S. Gouveia, P.C. Castilho, Analysis of phenolic compounds in leaves from endemic trees from Madeira Island. A contribution to the chemotaxonomy of Laurisilva forest species, *Ind. Crops Prod.* 64 (2015) 135–151, <https://doi.org/10.1016/J.INDCROP.2014.10.068>.
- [48] K.E. Pianoski, J.F. Turco, K.C.N. Soares, J.B. Mokochinski, I.K. Caetano, F.R. Da Silva, Y.R. Torres, Identification and characterization of bauhinia species by spectroscopic and spectrometric fingerprints identification and characterization of bauhinia species by spectroscopic and spectrometric fingerprints, *Revista Virtual de Química* 12 (2020) 1222–1235, <https://doi.org/10.21577/1984-6835.20200093>.
- [49] G. Negri, R. Tabach, Saponins, tannins and flavonols found in hydroethanolic extract from Perlandra dulcis roots, *Revista Brasileira de Farmacognosia* 23 (2013) 851–860, <https://doi.org/10.1590/S0102-695X2013000600001>.
- [50] E.T.D. Nobrega, K.C. de Araújo, A.J. Moreira, R.C. de Oliveira, G.T.S.T. da Silva, S. F. Blaskiewicz, L.L. Soares, S.G. Lemos, L.H. Mascaro, C.E. Pereira, Pure and cobalt-modified ZnO nanostructures prepared by a new synthesis route applied to

- environmental remediation, *J. Braz. Chem. Soc.* 35 (2024), <https://doi.org/10.21577/0103-5053.20240054> e-20240054.
- [51] N. Mayedwa, N. Mongwaketsi, S. Khamlich, K. Kaviyarasu, N. Matinise, M. Maaza, Green synthesis of nickel oxide, palladium and palladium oxide synthesized via *Aspalathus linearis* natural extracts: physical properties & mechanism of formation, *Appl. Surf. Sci.* 446 (2018) 266–272, <https://doi.org/10.1016/j.apsusc.2017.12.116>.
- [52] I. Fatimah, G. Purwiandono, H. Hidayat, S. Sagadevan, S.A.I.S.M. Ghazali, W. C. Oh, R.A. Doong, Flower-like SnO₂ nanoparticle biofabrication using *pometia pinnata* leaf extract and study on its photocatalytic and antibacterial activities, *Nanomaterials* 11 (2021) 3012, <https://doi.org/10.3390/NANO11113012>, 2021, Vol. 11, Page 3012.
- [53] N. Matinise, K. Kaviyarasu, N. Mongwaketsi, S. Khamlich, L. Kotsedi, N. Mayedwa, M. Maaza, Green synthesis of novel zinc iron oxide (ZnFe₂O₄) nanocomposite via *Moringa Oleifera* natural extract for electrochemical applications, *Appl. Surf. Sci.* 446 (2018) 66–73, <https://doi.org/10.1016/j.apsusc.2018.02.187>.
- [54] N. González-Ballesteros, P.M. Martins, C.J. Tavares, S. Lanceros-Méndez, Quercetin-mediated green synthesis of Au/TiO₂ nanocomposites for the photocatalytic degradation of antibiotic ciprofloxacin, *J. Ind. Eng. Chem.* (2024), <https://doi.org/10.1016/j.jiec.2024.09.003>.
- [55] Z. Li, W. Ma, I. Ali, H. Zhao, D. Wang, J. Qiu, Green and facile synthesis and antioxidant and antibacterial evaluation of dietary myricetin-mediated silver nanoparticles, *ACS Omega* 5 (2020) 32632, <https://doi.org/10.1021/ACSOMEGA.0C05002>.
- [56] B. Ahmmad, K. Leonard, M. Shariful Islam, J. Kurawaki, M. Muruganandham, T. Ohkubo, Y. Kuroda, Green synthesis of mesoporous hematite (α-Fe₂O₃) nanoparticles and their photocatalytic activity, *Adv. Powder Technol.* 24 (2013) 160–167, <https://doi.org/10.1016/j.apt.2012.04.005>.
- [57] M. Thommes, K. Kaneko, A.V. Neimark, J.P. Olivier, F. Rodriguez-Reinoso, J. Rouquerol, K.S.W. Sing, Physisorption of gases, with special reference to the evaluation of surface area and pore size distribution (IUPAC Technical Report), *Pure Appl. Chem.* 87 (2015) 1051–1069, <https://doi.org/10.1515/pac-2014-1117>.
- [58] M.M. Teixeira, Y.G. Gobato, L. Gracia, L.F. da Silva, W. Avansi, M. Assis, R.C. de Oliveira, G.A. Prando, J. Andrés, E. Longo, Towards a white-emitting phosphor Ca₁₀V₆O₂₅ based material, *J. Lumin.* 220 (2020) 116990, <https://doi.org/10.1016/j.jlumin.2019.116990>.
- [59] B.D. Ngom, T. Mpahane, E. Manikandan, M. Maaza, ZnO nano-discs by lyophilization process: size effects on their intrinsic luminescence, *J. Alloys Compd.* 656 (2016) 758–763, <https://doi.org/10.1016/j.jallcom.2015.09.230>.
- [60] H.A. Alburaih, S. Aman, N. Ahmad, S.R. Ejaz, R.Y. Khosa, A.G. Abid, S. Manzoor, H. M.T. Farid, M.S. Waheed, T.A. Taha, Synergistic photodegradation of methylene blue by Sm doped Fe₂O₃ photocatalyst under sunlight, *Chin. J. Phys.* 83 (2023) 637–649, <https://doi.org/10.1016/j.cjph.2022.08.017>.
- [61] P. García-Muñoz, N.P. Zussblatt, G. Pliego, J.A. Zazo, F. Fresno, B.F. Chmelka, J. A. Casas, Evaluation of photoassisted treatments for norfloxacin removal in water using mesoporous Fe₂O₃-TiO₂ materials, *J. Environ. Manag.* 238 (2019) 243–250, <https://doi.org/10.1016/j.jenvman.2019.02.109>.
- [62] M. Sayed, L.A. Shah, J.A. Khan, N.S. Shah, J. Nisar, H.M. Khan, P. Zhang, A. R. Khan, Efficient photocatalytic degradation of norfloxacin in aqueous media by hydrothermally synthesized immobilized TiO₂/Ti films with exposed (001) facets, *J. Phys. Chem. A* 120 (2016) 9916–9931, https://doi.org/10.1021/ACS.jpca.6B09719/SUPPL_FILE/JP6B09719_SI_001.PDF.
- [63] W. Liu, T. He, Y. Wang, G. Ning, Z. Xu, X. Chen, X. Hu, Y. Wu, Y. Zhao, Synergistic adsorption-photocatalytic degradation effect and norfloxacin mechanism of ZnO/ZnS@BC under UV-light irradiation, *Sci. Rep.* 10 (1 10) (2020) 1–12, <https://doi.org/10.1038/s41598-020-68517-x>, 2020.
- [64] Z. Liu, X. Yu, F. Yang, K. Wang, J. Zhang, N. Zhao, L. Chen, J. Niu, Synthesis of Co-doped Cu₂O particles and evaluation of their photocatalytic activity in the degradation of norfloxacin, *ChemistrySelect* 7 (2022) e202203682, <https://doi.org/10.1002/slct.202203682>.
- [65] A.A. Mashentseva, D.T. Nurpeisova, M. Barsbay, Effect of copper doping on the photocatalytic performance of Ni₂O₃@PC membrane composites in norfloxacin degradation, *RSC Adv.* 14 (2024) 4424–4435, <https://doi.org/10.1039/D3RA07471D>.
- [66] J. Patel, A.K. Singh, S.A.C. Carabineiro, Assessing the photocatalytic degradation of fluoroquinolone norfloxacin by Mn:ZnS quantum dots: kinetic study, degradation pathway and influencing factors, *Nanomaterials* 10 (2020) 964, <https://doi.org/10.3390/NANO10050964>, 2020, Vol. 10, Page 964.
- [67] D. Song, M. Li, L. Liao, L. Guo, H. Liu, B. Wang, Z. Li, High-crystallinity BiOCl nanosheets as efficient photocatalysts for norfloxacin antibiotic degradation, *Nanomaterials* 13 (2023) 1841, <https://doi.org/10.3390/NANO13121841>, 2023, Vol. 13, Page 1841.
- [68] C.-K. Huang, T. Wu, C.-W. Huang, C.-Y. Lai, M.-Y. Wu, Y.-W. Lin, Enhanced photocatalytic performance of BiVO₄ in aqueous AgNO₃ solution under visible light irradiation, *Appl. Surf. Sci.* 399 (2017) 10–19, <https://doi.org/10.1016/j.apsusc.2016.12.038>.
- [69] I. Mahboob, I. Shafiq, S. Shafique, P. Akhter, U.-S. Amjad, M. Hussain, Y.-K. Park, Effect of active species scavengers in photocatalytic desulfurization of hydrocracker diesel using mesoporous Ag₃VO₄, *Chem. Eng. J.* 441 (2022) 136063, <https://doi.org/10.1016/j.cej.2022.136063>.
- [70] S. Garg, Y. Yuan, M. Mortazavi, T.D. Waite, Caveats in the use of tertiary butyl alcohol as a probe for hydroxyl radical involvement in conventional ozonation and catalytic ozonation processes, *ACS ES&T Engineering* 2 (2022) 1665–1676, <https://doi.org/10.1021/acsestengg.2c00059>.
- [71] B.D. Ngom, T. Mpahane, N. Manyala, O. Nemraoui, U. Buttner, J.B. Kana, A. Y. Fasasi, M. Maaza, A.C. Beye, Structural and optical properties of nano-structured tungsten-doped ZnO thin films grown by pulsed laser deposition, *Appl. Surf. Sci.* 255 (2009) 4153–4158, <https://doi.org/10.1016/j.apsusc.2008.10.122>.
- [72] M. Maaza, K. Bouziane, J. Maritz, D.S. McLachlan, R. Swanepool, J.M. Frigerio, M. Every, Direct production of thermochromic VO₂ thin film coatings by pulsed laser ablation, *Opt. Mater.* 15 (2000) 41–45, [https://doi.org/10.1016/S0925-3467\(99\)00104-4](https://doi.org/10.1016/S0925-3467(99)00104-4).
- [73] S. Ekambaram, M. Maaza, Combustion synthesis and luminescent properties of Eu³⁺-activated cheap red phosphors, *J. Alloys Compd.* 395 (2005) 132–134, <https://doi.org/10.1016/j.jallcom.2004.09.075>.
- [74] J. Sithole, B.D. Ngom, S. Khamlich, E. Manikanadan, N. Manyala, M.L. Saboungi, D. Knoessen, R. Nemetudi, M. Maaza, Simonkolleite nano-platelets: synthesis and temperature effect on hydrogen gas sensing properties, *Appl. Surf. Sci.* 258 (2012) 7839–7843, <https://doi.org/10.1016/j.apsusc.2012.04.073>.